Larger and denser: an optimal design for surface grids of EMG electrodes to identify greater and more representative samples of motor units

Arnault H. Caillet[1,2,+], Simon Avrillon[1,+], Aritra Kundu[1], Tianyi Yu[1], Andrew T.M. Phillips[2], Luca Modenese[3], Dario Farina[1]*

[1]Department of Bioengineering, Imperial College London, SW7 2AZ, UK
[2]Department of Civil and Environmental Engineering, Imperial College London, SW7 2AZ, UK
[3]Graduate School of Biomedical Engineering, University of New South Wales, Sydney, Australia

[+] These authors contributed equally to the study and share the first authorship.

* Corresponding author
Prof. Dario Farina
Sir Michael Uren Hub
Imperial College London
86 Wood Ln
London W12 0BZ
E-mail address: d.farina@imperial.ac.uk
ORCID: 0000-0002-7883-2697

Running title: HD-EMG decomposition with larger and denser grids

All the authors in this paper have no financial or other relationships that might lead to a conflict of interest.

Abstract

The spinal motor neurons are the only neural cells whose individual activity can be non-invasively identified using grids of electromyographic (EMG) electrodes and source separation methods, i.e., EMG decomposition. In this study, we combined computational and experimental approaches to assess how the design parameters of grids of electrodes influence the number and characteristics of the motor units identified. We first computed the percentage of unique motor unit action potentials that could be theoretically discriminated in a pool of 200 simulated motor units when recorded with grids of various sizes and interelectrode distances (IED). We then identified motor units from experimental EMG signals recorded in six participants with grids of various sizes (range: 2-36 cm^2) and IED (range: 4-16 mm). Increasing both the density and the number of electrodes, as well as the size of the grids, increased the number of motor units that the EMG decomposition could theoretically discriminate, i.e., up to 82.5% of the simulated pool (range: 30.5-82.5%). Experimentally, the configuration with the largest number of electrodes and the shortest IED maximized the number of motor units identified (56 ± 14; range: 39-79) and the percentage of low-threshold motor units identified (29 ± 14%). Finally, we showed with a prototyped grid of 400 electrodes (IED: 2 mm) that the number of identified motor units plateaus beyond an IED of 2-4 mm. These results showed that larger and denser surface grids of electrodes help to identify a larger and more representative pool of motor units than currently reported in experimental studies.

Significance statement

Individual motor unit activities can be exactly identified by blind-source separation methods applied to multi-channel EMG signals recorded by grids of electrodes. The design parameters of grids of EMG electrodes have never been discussed and are usually arbitrarily fixed, often based on commercial availability. In this study, we showed that using larger and denser grids of electrodes than conventionally applied can drastically increase the number of motor units identified. These samples of motor units are moreover more balanced between high- and low- threshold motor units and provide a more representative sampling of neural drive to muscles. Gathering large datasets of motor units using large and dense grids will impact the study of motor control, neuromuscular modelling, and human-machine interfacing.

Introduction

Decoding the neural control of natural behaviours relies on the identification of the discharge activity of individual neural cells. Classically, arrays of electrodes are implanted close to the cells to record their electrical activity. The application of algorithms that separate the overlapping activity of these cells has enabled researchers to study neural processes in multiple areas of the brain (Stringer et al., 2019), such as in the motor or the sensorimotor areas (Churchland and Shenoy, 2007; Gallego et al., 2020). At the periphery of the nervous system, it is also possible to record the activity of individual motor neurons innervating muscle fibres (Heckman and Enoka, 2012; Farina et al., 2016; Enoka, 2019). The motor unit, i.e., a motor neuron and the fibres it innervates, acts as an amplifier of the neural activity, as one action potential propagating along a motor neuron's axon generates an action potential in each of the innervated muscle fibres. The activity of motor units can be identified by decomposing surface electromyographic (EMG) signals into trains of motor unit action potentials (MUAPs) using blind-source separation algorithms (Holobar and Farina, 2014; Farina and Holobar, 2016). The multiple observations for source separation are obtained by recording EMG signals with grids of electrodes. This approach usually allows for the reliable analysis of 5 to 40 concurrently active motor units (Del Vecchio et al., 2017; Del Vecchio et al., 2020; Hug et al., 2021a).

While the design of intracortical (e.g., (Jun et al., 2017; Steinmetz et al., 2018)) and intramuscular (e.g., (Muceli et al., 2015; Muceli et al., 2022)) arrays of electrodes has scaled up over the years to record larger samples of neural cells, the configuration of surface EMG grids of electrodes has not systematically evolved. Most researchers currently use grids with 64 electrodes arranged in 13 × 5 or 8 × 8 montages, the interelectrode distance (IED) between adjacent electrodes (e.g., 4 mm, 8 mm, or 10 mm) being dictated by the size of the muscle to cover. Yet, optimizing these parameters, i.e., grid size and IED, may influence the performance of EMG decomposition. Currently, there are no recommendations on optimal design parameters for grids when using surface EMG for the study of motor units.

Source separation algorithms are based on the necessary condition that identifiable motor units have unique representations across the multi-channel EMG signal (Farina et al., 2008; Holobar and Farina, 2014; Farina and Holobar, 2016). This implies that the three-dimensional waveform of a MUAP (one time dimension and two spatial dimensions) should be unique within the pool of motor units detected by the surface grid. In practice, the identified motor units are those that innervate larger numbers of muscle fibres, as their action potentials tend to have the largest energy. Conversely, low-threshold motor units usually remain hidden since their energy is close to the baseline noise. Increasing the density of electrodes would increase the spatial sampling frequencies of the EMG signals (Farina and Holobar, 2016). This should improve the discrimination of MUAPs, allowing the identification of a larger number of motor units. Additionally, increasing the electrode density may reveal the hidden low-threshold motor units by sampling their action potentials across a larger number of electrodes, leading to a better compensation of the additive noise in the mixture model of the EMG signal.

In this study, we combined computational and laboratory experiments to identify the optimal design criteria for grids of surface electrodes with the aim of maximizing the number of identified motor units, specifically increasing the relative number of identifiable low-threshold motor units. We first simulated a pool of 200 motor units and the associated EMG signals recorded from grids of electrodes of various sizes and densities. These simulations showed that the greater the size and the density of the grid, the higher the percentage of identifiable motor units and the relative ratio of identifiable small and deep units. We confirmed these theoretical results with experimental signals recorded with a grid of 256 electrodes with a 4-mm IED that was downsampled in the space domain to obtain six grid configurations (surface range: 2-36 cm^2 and IED range: 4-16 mm). Finally, we prototyped a new grid of 400 electrodes with a 2-mm IED and demonstrated that the number of identified motor units approximately plateaus beyond a 2-4-mm IED.

Methods

Computational study

A pool of 200 motor units was simulated to test whether increasing the density and the size of surface grids of electrodes would impact the number of identifiable motor units. The simulations were based on an anatomical model of a cylindrical muscle volume with parallel fibres (Farina et al., 2008; Konstantin et al., 2020), where subcutaneous and skin layers separate the muscle from the surface electrodes. Specifically, we set the radius of the muscle to 25.4 mm and the thicknesses of the subcutaneous and skin layers to 5 mm and 1 mm, respectively. The centres of the motor units were distributed within the cross section of the muscle using a farthest point sampling. The farthest point sampling filled the cross-section by iteratively adding centres points that were maximally distant from all the previously generated motor unit centres, resulting in a random and even distribution of the motor unit territories within the muscle. The number of fibres innervated by each motor neuron followed an exponential distribution, ranging from 15 to 1500. The fibres of the same motor unit were positioned around the centre of the motor unit within a radius of 0.0082 to 0.8 mm, and a density of 20 fibres/mm^2. Because motor unit territories were intermingled, the density of fibres in the muscle reached 200 fibres/mm^2. The MUAPs were detected by circular surface electrodes with a diameter of 1 mm. The simulated grids were centred over the muscle in the transverse direction, with a size ranging from 14.4 to 36 cm^2, and an IED ranging from 2 to 36 mm.

Laboratory study

<u>Participants</u>

Six healthy participants (all males; age: 26 ± 4 yr; height: 174 ± 7 cm; body weight: 66 ± 15 kg) volunteered to participate in the first experimental session of the study. They had no history of lower limb injury or pain during the months preceding the experiments. One of these individuals (age: 26 yr; height: 168 cm; bodyweight: 51 kg) participated in a second experimental session to test the prototyped grid with an IED of 2 mm. The Ethics Committee at Imperial College London reviewed and approved all procedures and protocols (no. 18IC4685). All participants provided their written informed consent before the beginning of the experiment.

<u>Experimental tasks</u>

The two experimental sessions consisted of a series of isometric ankle dorsiflexions performed at 30% and 50% of the maximal voluntary torque (MVC) during which we recorded high density electromyographical (HD-EMG) signals over the Tibialis Anterior muscle (TA). The participants sat on a massage table with the hips flexed at 30°, 0° being the hip neutral position, and their knees fully extended. We fixed the foot of the dominant (right in all participants) leg onto the pedal of a commercial dynamometer (OT Bioelettronica, Turin, Italy) positioned at 30° in the plantarflexion direction, 0° being the foot perpendicular to the shank. The thigh was fixed to the massage table with an inextensible 3-cm-wide Velcro strap. The foot was fixed to the pedal with inextensible straps positioned around the proximal phalanx, metatarsal and cuneiform. Force signals were recorded with a load cell (CCT Transducer s.a.s, Turin, Italy) connected in-series to the pedal using the same acquisition system as for the HD-EMG recordings (EMG-Quattrocento; OT Bioelettronica). The dynamometer was positioned accordingly to the participant's lower limb length and secured to the massage table to avoid any motion during the contractions.

All experiments began with a warm-up, consisting of brief and sustained ankle dorsiflexion performed at 50% to 80% of the subjective MVC. During the warm-up, all participants learnt to produce isometric ankle dorsiflexion without co-contracting the other muscles crossing the hip and knee joints. At the same time, we iteratively adjusted the tightening and the position of the straps to maximize the comfort of the participant. Then, each participant performed two 3-to-5 s MVC with 120 s of rest in between. The peak force value was calculated using a 250-ms moving average window, and then used to set the target level during the submaximal contractions. After 120 s of rest, each participant performed two trapezoidal contractions at 30% and 50% MVC with 120 s of rest in between, consisting of linear ramps up and down performed at 5%/s and a plateau maintained for 20 s and 15 s at 30% and 50% MVC, respectively. The order of the contractions was randomized. One participant (S2) did not perform the contractions at 50% MVC.

<u>High-density electromyography</u>

In the first experimental session, four adhesive grids of 64 electrodes (13 x 5; gold coated; 1 mm diameter; 4 mm IED; OT Bioelettronica) were placed over the belly of the TA. The grids were carefully positioned side-to-side with a 4-mm-distance between the electrodes at the edges of adjacent grids (Figure 1A). The 256 electrodes were centred to the muscle belly and laid within the muscle perimeter identified through palpation. The skin was shaved, abrased and cleansed with 70% ethyl alcohol. Electrode-to-skin contact was maintained with a bi-adhesive perforated foam layer filled with conductive paste. The grids were wrapped with tape and elastic bands to secure the contact with the skin. The four 64-pre-amplifiers were connected in-series with stackable cables to a wet reference band placed above the medial malleolus of the same leg. HD-EMG signals were recorded in monopolar derivation with a sampling frequency of 2,048 Hz, amplified (x150), band-pass filtered (10–500 Hz), and digitised using a 400 channels acquisition system with a 16-bit resolution (EMG-Quattrocento; OT Bioelettronica).

In the second experimental session, one ultra-dense custom-made grid of 400 dry electrodes (20 x 20; gold coated; 0.5 mm diameter; 2 mm IED) was placed over the belly of the TA. The skin was first shaved and cleansed with abrasive paste. Then, the electrode was directly placed on the skin after the skin was wetted to decrease the impedance between the skin and the dry electrodes. The HD-EMG signals were then recorded in monopolar mode with a sampling frequency of 2,048 Hz, following the same procedure as before with eight 64-pre-amplifiers connected in-series with stackable cables to a wet reference band placed above the medial malleolus of the same leg.

Grid configurations

During the first experimental session, we recorded the myoelectric activity of the TA with a total of 256 electrodes covering 36 cm^2 of the muscle surface (10 cm x 3.6 cm, 4-mm IED, Figure 1A). To investigate the effect of the electrode density, we downsampled the 256-electrode grid by successively discarding rows and columns of electrodes and artificially generating three new grids covering the same area with IEDs 8 mm, 12 mm, and 16 mm, involving 256, 64, 35, and 20 electrodes, respectively (Figure 1B-D). It is noteworthy that the 8-mm and 16-mm grids covered a surface of 32 cm^2 because they included an odd number of rows and columns. To investigate the effect of the size of the grid, we discarded the peripherical electrodes to generate grids of 63, 34 and 19 electrodes with a 4-mm IED, covering 7.7, 3.8 and 2 cm^2 of the muscle (Figure 1E-G). Note that we chose these grid sizes to match the number of electrodes used in the density analysis, thus comparing grids with similar number of electrodes, but different densities and sizes (in Figure 1, B versus E, and C versus F).

During the second experimental session, we recorded the myoelectric activity of the TA with the ultra-dense grid of 400 dry electrodes covering 16 cm^2 of the muscle (4 cm x 4 cm, 2-mm IED). Using the same procedure as above, we generated two artificial grids with an IED of 4 mm and 8 mm, and 100 and 25 electrodes, respectively.

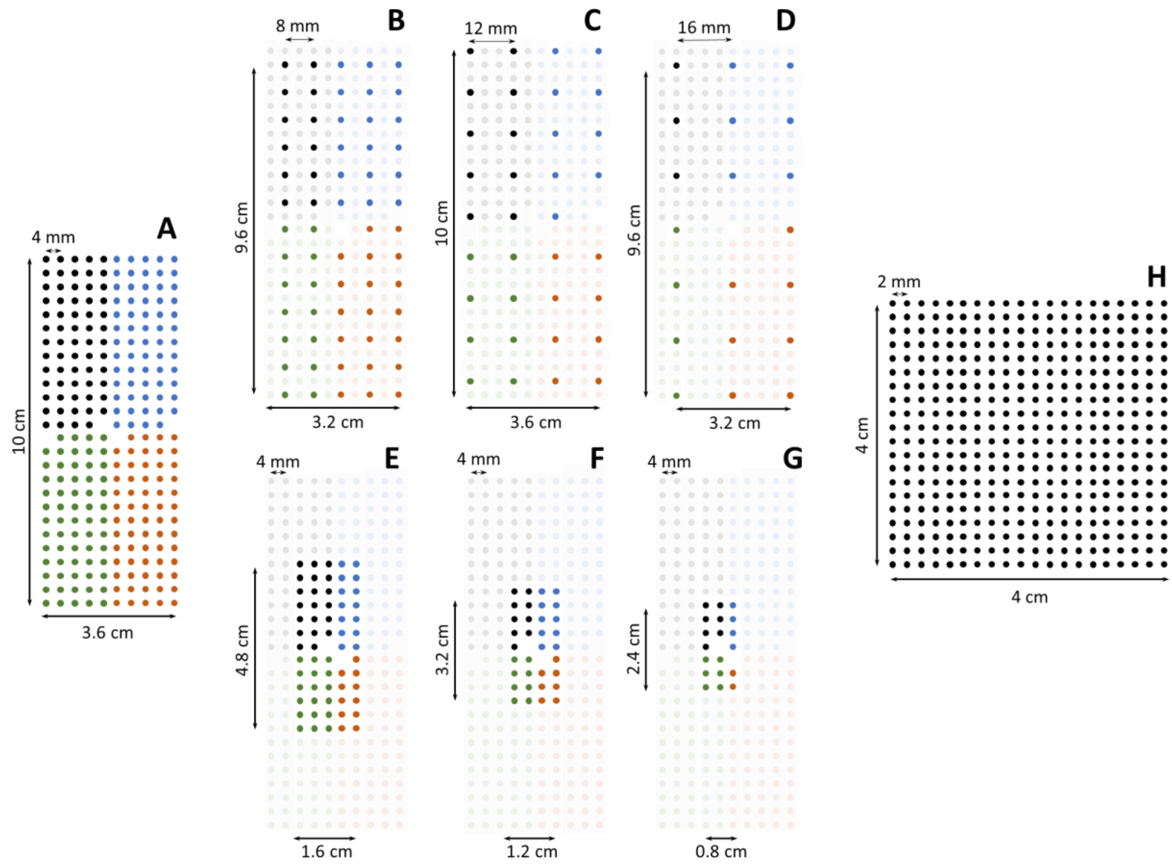

Figure 1: The eight grid configurations considered in this study. From the grid of 256 electrodes (A, grid size: 36 cm^2, IED: 4 mm), six shallower and smaller grids (B-G) were artificially obtained by discarding the relevant electrodes and used in the first experimental session. (B,C,D) Density analysis: 8, 12, and 16mm IED. (E,F,G) Size analysis: 7.7, 3.6, and 2 cm^2 surface area. (H) The ultra-dense grid of 400 dry electrodes (grid size: 16 cm^2, IED: 2 mm) used in the second experimental session.

HD-EMG decomposition

We decomposed the signals recorded in all the conditions using the same parameters and procedure. First, the monopolar EMG signals were bandpass filtered between 20-500 Hz with a second-order Butterworth filter. After visual inspection, channels with low signal-to-noise ratio or artifacts were discarded. The HD-EMG signals were then decomposed into motor unit spike trains using convolutive blind-source separation, as previously described (Negro et al., 2016). In short, the EMG signals were first extended to reach 1000 channels and spatially whitened. Thereafter, a fixed-point algorithm that maximized the sparsity was applied to identify the sources embedded in the EMG signals, i.e., the series of delta functions centred at the motor unit discharge times. These sources are sparse, with most samples being 0 (i.e., absence of discharge) and a small number of samples being 1 (i.e., discharge times). In this algorithm, a contrast function was iteratively applied to the EMG signals to estimate the level of sparsity of the identified sources, and the convergence was reached once the level of sparsity did not vary when compared to the previous iteration, with a tolerance fixed at 10^{-4} (see Negro et al., 2016, for the definition of the detailed contrast functions). At this stage, the estimated source contained high peaks (i.e., the delta functions from the identified motor unit) and low peaks from other motor units and noise. High peaks were separated from low peaks and noise using peak detection and K-mean classification with two classes. The peaks from the class with the highest centroid were considered as the spikes of the identified motor unit. A second algorithm refined the estimation of the discharge times by iteratively recalculating the motor unit filter and repeating the steps with peak detection and K-mean classification until the coefficient of variation of the inter-spike intervals was minimized. This decomposition procedure has been previously validated using experimental and simulated signals (Negro et al., 2016). After the automatic identification of the motor units, duplicates were removed, and all the motor unit spike trains were visually checked for false positives and false negatives (Del Vecchio et al., 2020). This manual step is highly reliable across operators (Hug et al., 2021b). Only the motor units which exhibited a pulse-to-noise ratio (PNR) > 28 dB were retained for further analysis.

We further tested whether decomposing subsets of electrodes within a highly populated grid of 256 electrodes increased the number of identified motor units. Indeed, the lower ratio of large motor units sampled by each independent subset of 64 electrodes could allow the algorithm to converge to smaller motor units that contribute to the signal. For a similar number of iterations, it is likely that these motor units would have otherwise contributed to the noise component of the mixture model of the EMG signal (Farina and Holobar, 2016). Thus, we decomposed the four separated grids of 64 electrodes before removing the motor units duplicated between grids. Similarly, the grid with 400 electrodes was decomposed as eight separated partially overlapping subsets of 64 electrodes.

Analysis

Computational study

We first estimated the theoretical percentage of identifiable motor units for each of the simulated conditions. To do so, the simulated MUAPs detected over the entire set of electrodes were compared with each other. The comparisons were done pairwise by first aligning the MUAPs in time using the cross-correlation function, and then computing the normalised mean square difference between the aligned action potentials. Pairs of action potentials with a mean square difference below 5% were considered not discriminable. The 5% criterion was based on the variability of motor unit action potential shapes observed experimentally for individual motor units (Farina et al., 2008). After computing all pair-wise comparisons, we then computed the proportion of action potentials that could be discriminated from all others, i.e., the proportion of unique action potentials. This metrics is independent from the algorithm used for decomposition and establishes an upper bound in the number of motor units that can be identified by any decomposition algorithm. For each unique action potential, we also computed the distance between the centre of the territory of the corresponding muscle fibres and the skin surface.

Laboratory study – number of identified motor units

We reported the absolute number of motor units (PNR > 28 dB) identified with all the experimental grid configurations. For each participant, the number of identified motor units was then normalized to the maximal number of motor units found across all conditions, yielding normalized numbers of identified motor units $\overline{N}$ then expressed in percentage. For each condition, we calculated the mean and standard deviation of the $\overline{N}$ values across participants. To investigate the effects of density and size of the grid, we fitted logarithmic trendlines to the relationships between the averaged $\overline{N}$ values and IED and grid size. We also fitted a logarithmic trendline to the average $\overline{N}$ values and their corresponding number of electrodes, in which case the conditions involving the same number of electrodes, but different grid size and density, were given a weight of 0.5 in the minimization function. We reported the r^2 and p-value for each regression trendline. To maintain consistency with the computational study on the investigation of the maximum number of identifiable motor units depending on grid design, the trendlines were fitted on the results obtained when the complete grids of 256 electrodes were decomposed as independent subsets of 64 electrodes, which systematically returned the highest number of identified motor units. The trendlines fitted on the results obtained when all available signals were simultaneously decomposed are reported in Supplementary Material A.

Laboratory study – characteristics of identified motor units

To investigate the effects of electrode density and grid size on the characteristics of the motor unit identified, we used a typical frequency distribution of the motor unit force recruitment thresholds in the human TA (Caillet et al., 2022a), where $F^{th}(j)$ is the force recruitment threshold of the j^{th} motor unit in the normalized motor unit pool ranked in ascending order of F^{th}.

$$F^{th}(j) = 0.50 \cdot \left(58.12 \cdot j + 120^{j^{1.83}}\right), j \in [0; 1]$$

Based on their measured force recruitment threshold, the identified motor units were classified with this relationship to the first (‘low-threshold’ or ‘small’) or second (‘high-threshold’ or ‘large’) half of the active pool, consistent with the Henneman’s size principle (Henneman and Mendell, 1981; Caillet et al., 2022b). For each condition, we reported the percentage of identified motor units classified as ‘small’.

We did not report this metric when five or fewer motor units were identified in one condition for three or more participants.

<u>Laboratory study – correlation between observations</u>

We assessed how the density of electrodes impacted the information redundancy in the EMG signals recorded by adjacent electrodes. To this end, MUAP shapes were identified over the 256 electrodes with the spike-triggered averaging technique. To do so, the discharge times were used as a trigger to segment and average the HD-EMG signals over a window of 50 ms. For each motor unit, we identified the electrode with the highest MUAP peak-to-peak amplitude and calculated the average correlation coefficient ρ with the MUAPs recorded by the four adjacent electrodes using an IED of 4 mm, 8 mm, 12 mm, and 16 mm. We also repeated this correlation analysis for the ultra-dense grid of 400 electrodes using an IED of 2 mm, 4 mm, and 8 mm.

Results

Computational study

We simulated the firing activity of 200 motor units recorded by 84 configurations of grids of electrodes (Figure 2; surface range: 14.4 to 36 cm^2, IED range: 2 to 36 mm). The number of identifiable motor units increased with the surface size of the grid, from 49.9 ± 6.5% of the motor units identifiable with a grid of 14.4 cm^2 to 78.7 ± 2.6% of the motor units identifiable with a grid of 36 cm^2. The number of identifiable motor units also increased with a decrease in interelectrode distance. For example, with a grid of 36 cm^2, the number of identifiable motor units increased from 72% to 82.5% of the motor units with an IED of 36 and 2 mm, respectively (Figure 2B). Increasing the surface size and the density of the grid of electrodes revealed smaller and deeper motor units, with averaged territories radius of 0.165 and 0.149 mm with grids of 14.4 and 36 cm^2, respectively, and an IED of 2 mm (Figure 2C). The average distance of identifiable motor units from the skin increased with the surface size of the grid (Figure 2D; 15.7 ± 0.1 mm vs. 17.3 ± 0.1 mm with grids of 14.4 and 36 mm^2, respectively), but not with the IED of the grids (Figure 2D; 16.4 ± 0.6 mm vs. 16.3 ± 0.8 mm with an IED of 36 and 2 mm, respectively).

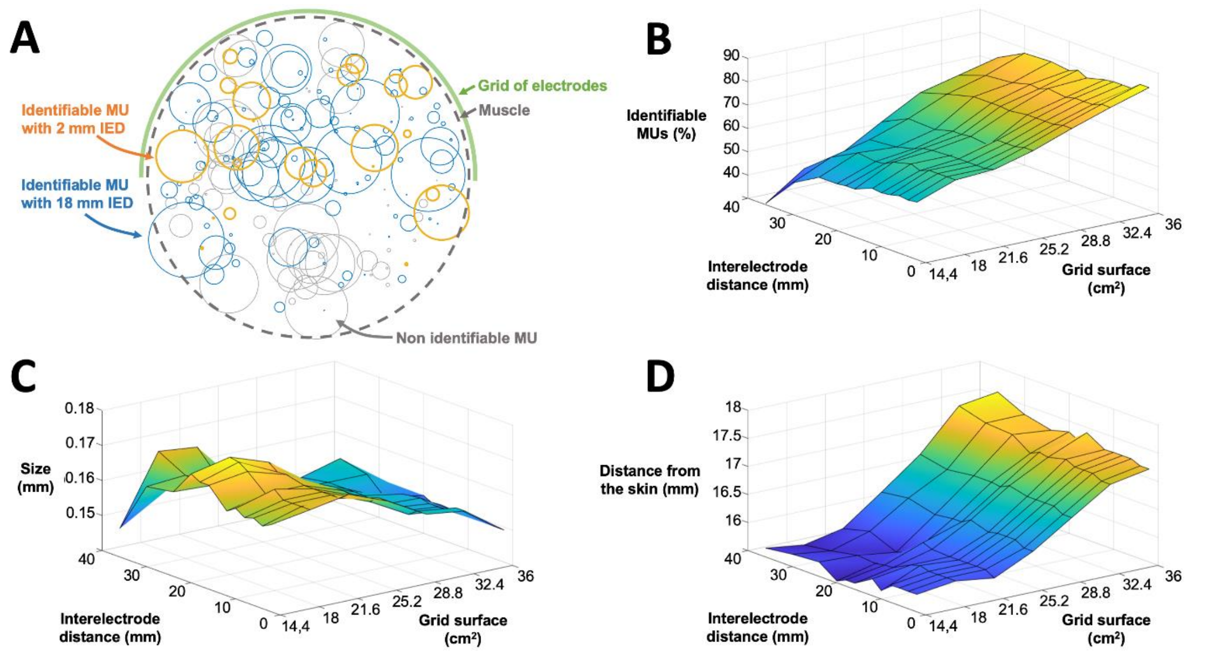

Figure 2: Results from the 200 simulated motor units with 84 configurations of grids of electrodes. (A) Each circle represents a motor unit territory, the dash line being the muscle boundary. Blues circles are the identifiable motor units with a grid of 21.6 cm^2 and an interelectrode distance (IED) of 18 mm, while the orange circles are the motor units revealed with a grid of 21.6 cm^2 and an IED of 2mm. Grey circles represent the non-identifiable motor units. The percentage of identifiable motor units (B), the size of their territory (C) and their distance from the skin (D) are reported for the 84 configurations.

Laboratory study - grids of 256 electrodes

<u>Number of identified motor units</u>

The motor unit spike trains identified across all conditions, intensities, and participants were visually checked and carefully edited when a missing spike or an identified artifact were observed. The highest number of identified motor units was systematically reached with the separate decomposition of the four grids of 64 electrodes with an IED of 4 mm, resulting in 56 ± 14 motor units (PNR = 34.2 ± 1.1) and 45 ± 10 motor units (PNR = 34.0 ± 0.9) for 30% and 50% MVC, respectively (Figure 3). At least 82% of the motor units identified in one condition were also identified in the conditions involving a higher number of electrodes. Similarly, 91% to 100% of the motor units identified in one condition were also identified with the 256-electrode configuration (4-mm IED, 36-cm^2 size, Figure 1A) when the four grids were decomposed separately.

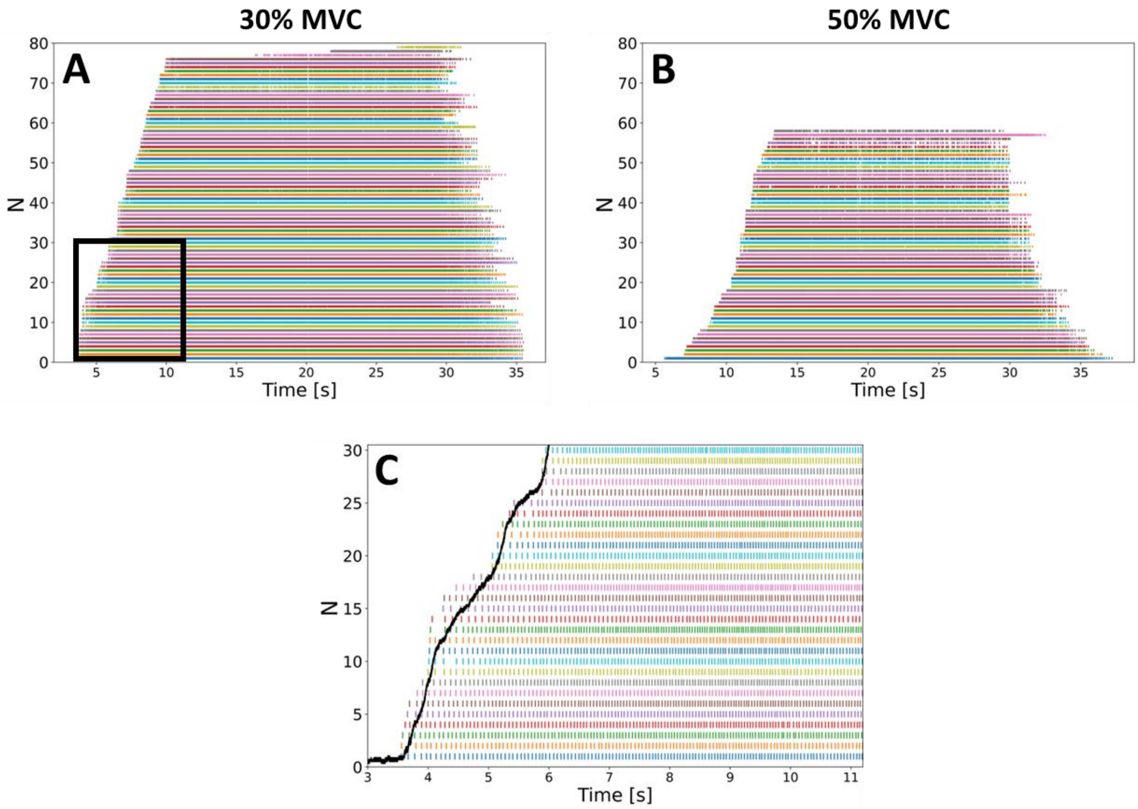

Figure 3: Maximum numbers of motor unit spike trains identified in one participant (S1) at 30% (A) and 50% MVC (B), 79 and 58 motor units (PNR > 28 dB) respectively, obtained when the four grids of 64 electrodes (4 mm IED) were decomposed separately. (C) The pulse trains of the 30 motor units of lowest recruitment threshold identified at 30% MVC (black box in A) are reproduced during the ascending ramp of force (black curve).

When considering the effect of electrode density (grid size fixed at 32-36 cm^2, Figure 1A-D), we found the lowest number N of motor units with the 16-mm IED, identifying 3 ± 1 motor units and 2 ± 1 motor units at 30% and 50% MVC, respectively (Figure 4A, C). Additional motor units were then gradually identified with greater electrode densities. The highest number of motor units was observed with the highest density (4-mm IED), respectively identifying 56 ± 14 or 43 ± 11 motor units and 45 ± 10 or 25 ± 6 motor units at 30% and 50% MVC, and this with the 4×64 or 256-electrode decomposition procedure (Figure 4A, C). Finally, we found a decreasing logarithmic relationship between the average normalized number $\overline{N}$ of motor units for each participant and the IED, with $r^2 = 1.0$ ($p = 2.5 \cdot 10^{-5}$) and $r^2 = 0.99$ ($p = 0.001$) at 30% and 50% MVC, respectively (Figure 4B, D).

When considering the effect of the size of the grid (IED fixed at 4 mm, Figure 1A, E-G), we found the lowest number N of motor units with a grid of 2 cm^2, identifying 4 ± 2 motor units and 4 ± 2 motor units at 30% and 50% MVC, respectively (Figure 5A, C). Additional motor units were then gradually identified with larger grid sizes. The highest number of motor units was observed with a grid of 36 cm^2, respectively identifying 56 ± 14 or 43 ± 11 motor units and 45 ± 10 or 25 ± 6 motor units at 30% and 50% MVC, depending on the decomposition procedure (Figure 5A, C). We also found an increasing logarithmic relationship between the average normalized number $\overline{N}$ of motor units for each participant and the size of the grid, with $r^2 = 0.99$ ($p = 3.0 \cdot 10^{-4}$) and $r^2 = 0.98$ ($p = 0.001$) at 30% and 50% MVC, respectively (Figure 5B, D). It is noteworthy that, in both density and size cases, the parameters of the fits were very similar for 30% and 50% MVC.

As both the density and the size of the grids determine the number of electrodes, we finally fitted the relationship between the normalized number of motor units $\overline{N}$ and the number of electrodes. As observed previously, more motor units were identified with a larger number of electrodes, following a logarithmic tendency with $r^2 = 0.98$ ($p = 0.018$) and $r^2 = 0.95$ ($p = 0.016$) at 30% and 50% MVC, respectively (Figure 6). A plateau should theoretically be reached with highly populated grids of 1024 and 4096 electrodes (36-cm^2 grids with 2-mm and 1-mm IED, respectively), with a prediction of 50% and 90% of additional motor units identified.

For a fixed number of electrodes, it is noteworthy that grid size and density, although linked, may have different impact on the number of identified motor units (black crosses in Figure 6). For example, 1.25 times more motor units were obtained with the 64-electrode condition (32 cm^2, 8-mm IED, Figure 1B) than with the 63-electrode condition (7.7 cm^2, 4-mm IED, Figure 1E) for the group of participants at 30% MVC.

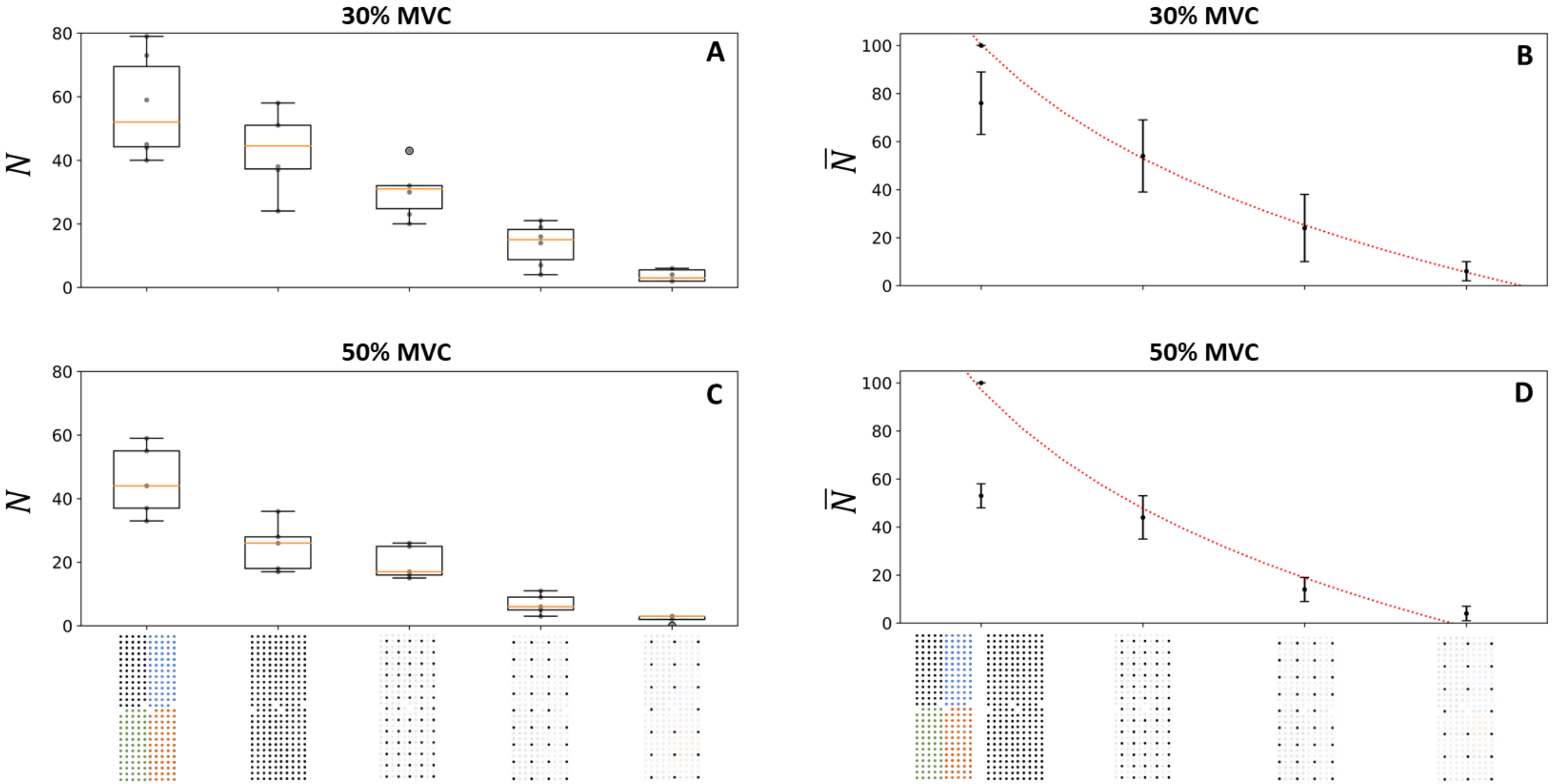

Figure 4: Effect of the electrode density on the number N of identified motor units at 30% (A, B) and 50% MVC (C, D). The boxplots in the left column report the absolute number N of identified motor units per participant (grey dots) and the median (orange line), quartiles, and 95%-range across participants. In the right column, the normalized number of motor units $\overline{N}$ logarithmically decreases with interelectrode distance d (4, 8, 12, and 16mm in abscissa) as $\overline{N} = 195 - 68\,log(d)$ $(r^2 = 1.0, p = 2.5 \cdot 10^{-5})$ at 30% MVC (B) and $\overline{N} = 196 - 71\,log(d)$ $(r^2 = 0.99, p = 0.001)$ at 50% MVC (D). The standard deviation of $\overline{N}$ across subjects is displayed with vertical bars. Two decomposition procedures were considered for the 256-electrode condition; the grid of 256 black electrodes indicates that the 256 signals were simultaneously decomposed and systematically returned lower $\overline{N}$ results than when the grid was decomposed as four subsets of 64 electrodes. To maintain consistency with the computational study, the trendlines were here fitted with the 4*64 condition that returned the higher number of identified motor units (see Supplementary Material A for the other fitting condition).

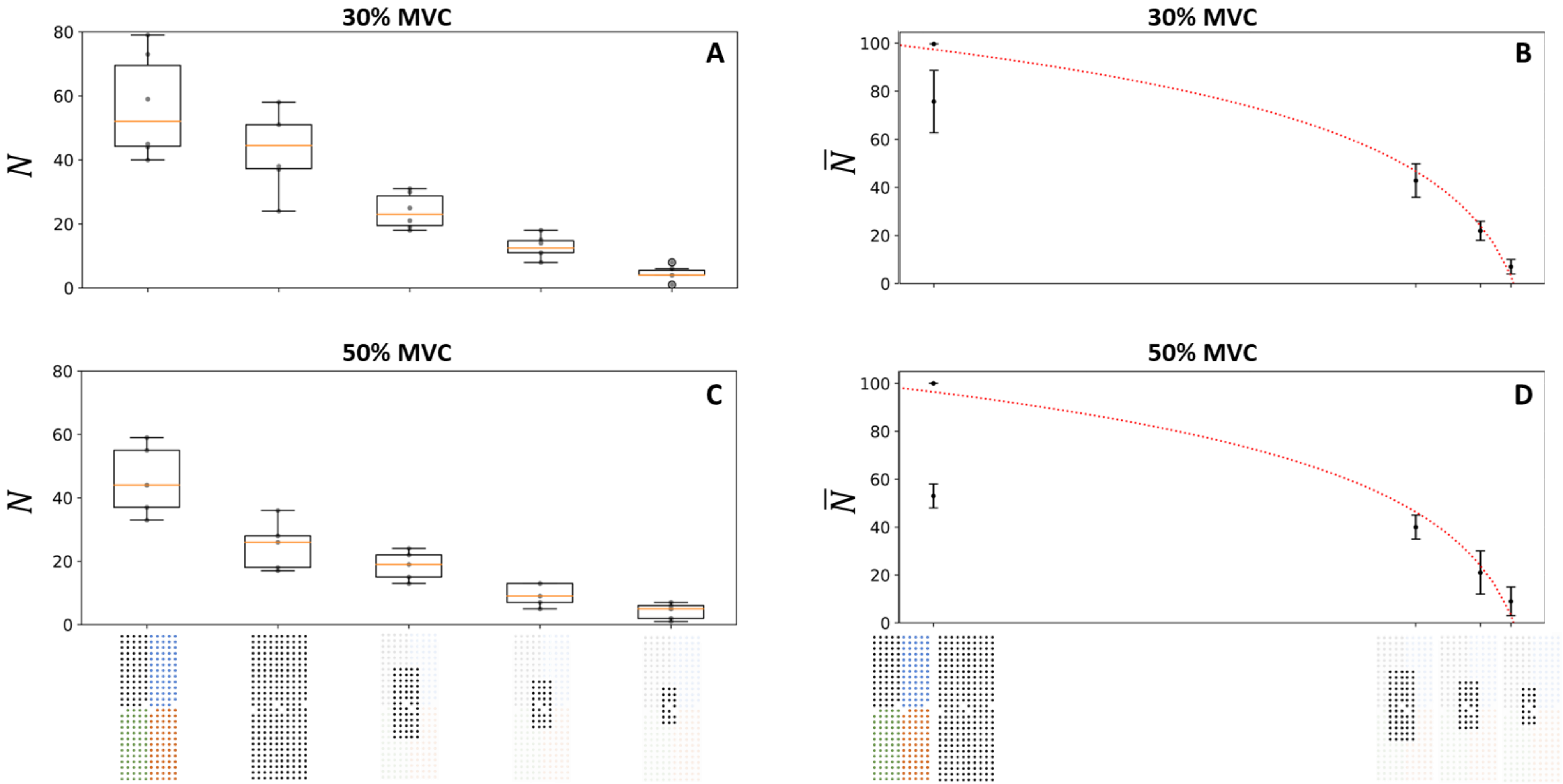

Figure 5: Effect of the size of the grid on the number N of identified motor units at 30% (A, B) and 50% MVC (C, D). The boxplots in the left column report the absolute number N of identified motor units per participant (grey dots) and the median (orange line), quartiles, and 95%-range across participants. In the right column, the normalized number of motor units $\overline{N}$ logarithmically decreases with the size of the grid s (2, 3.8, 7.7, and 36 cm^2 in abscissa) as $\overline{N} = -20 + 33\,log(s)$ $(r^2 = 0.99, p = 3.0 \cdot 10^{-4})$ at 30% MVC (B), and $\overline{N} = -19 + 32\,log(s)$ $(r^2 = 0.98, p = 0.001)$ at 50% MVC (D). The standard deviation of $\overline{N}$ across subjects is displayed with vertical bars. Two decomposition procedures were considered for the 256-electrode condition; the grid of 256 black electrodes indicates that the 256 signals were simultaneously decomposed and systematically returned lower $\overline{N}$ results than when the grid was decomposed as four subsets of 64 electrodes. To maintain consistency with the computational study, the trendlines were here fitted with the 4*64 condition that returned the higher number of identified motor units (see Supplementary Material A for the other fitting condition).

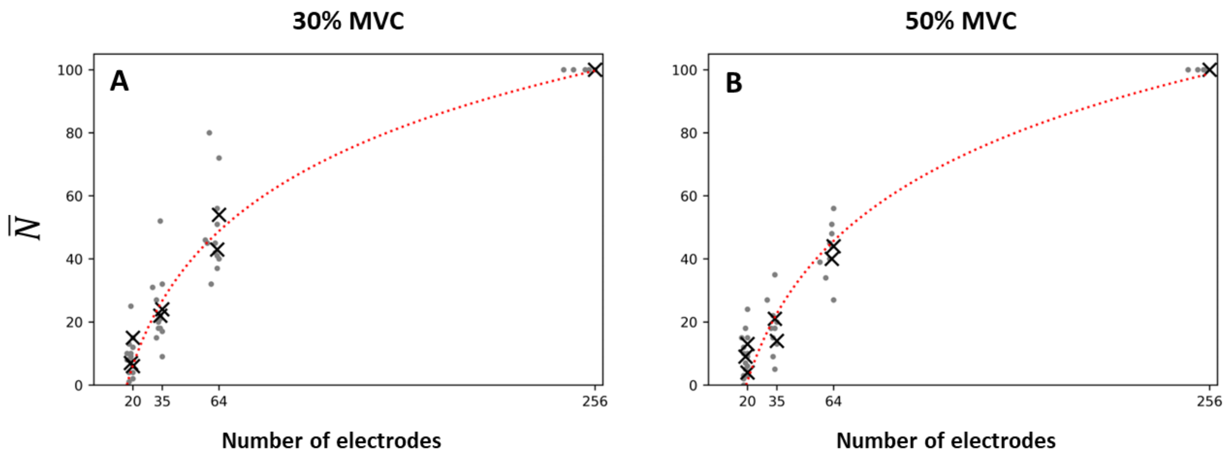

Figure 6: Effect of the number n of electrodes on the normalized number $\overline{N}$ of identified motor units at 30% (A) and 50% MVC (B). The discrete results per participant are displayed with grey data points. The average $\overline{N}$ values across participants per condition are displayed with black crosses. Weighted logarithmic trendlines were fitted to the data and returned (A) $\overline{N} = -104 + 37\,log(n)$ ($r^2 = 0.98, p = 0.018$), and (B) $\overline{N} = -113 + 38\,log(n)$ ($r^2 = 0.95,\ p = 0.016$). Two decomposition procedures were considered for the 256-electrode condition; the grid of 256 black electrodes indicates that the 256 signals were simultaneously decomposed and systematically returned lower $\overline{N}$ results than when the grid was decomposed as four subsets of 64 electrodes. To maintain consistency with the computational study, the trendlines were here fitted with the 4*64 condition that returned the higher number of identified motor units (see Supplementary Material A for the other fitting condition).

Characteristics of identified motor units

Figure 7A shows the effect of the grid density on the type (small/large) of identified motor units at 30% MVC, with a percentage of identified 'small' motor units increasing from 11 ± 9%, with a 12-mm IED, to 29 ± 14%, with a 4-mm IED. Such differences were not observed at 50% MVC, where the percentage of 'small' motor units remained below 10% for all conditions (Figure 7C). Contrary to the density, the size of the grid did not impact the distribution of the type of identified motor units, with the percentage of 'small' motor units ranging from 20 to 29% across all grid sizes (Figure 7B). Again, small motor units represented less than 10% of the identified motor units at 50% MVC for all the size conditions (Figure 7D).

To support the above observations made at 30% MVC, grids involving the same number of electrodes but of different grid density and size were directly compared. 62% of the motor units identified with the 64-electrode (32 cm^2, IED 8 mm) and 63-electrode (7.7 cm^2, IED 4 mm) conditions were identified by both grids at 30%. 28 ± 9% of the remaining motor units specific to the 8-mm IED grid were 'small', while 44 ± 11% of the motor units specific to the 4-mm IED condition were 'small'. Similar results were obtained with the 35- (36 cm^2, 12-mm IED) and 34-electrode conditions (3.6 cm^2, 4-mm IED), where more 'small' motor units were specifically identified with denser rather than larger grids.

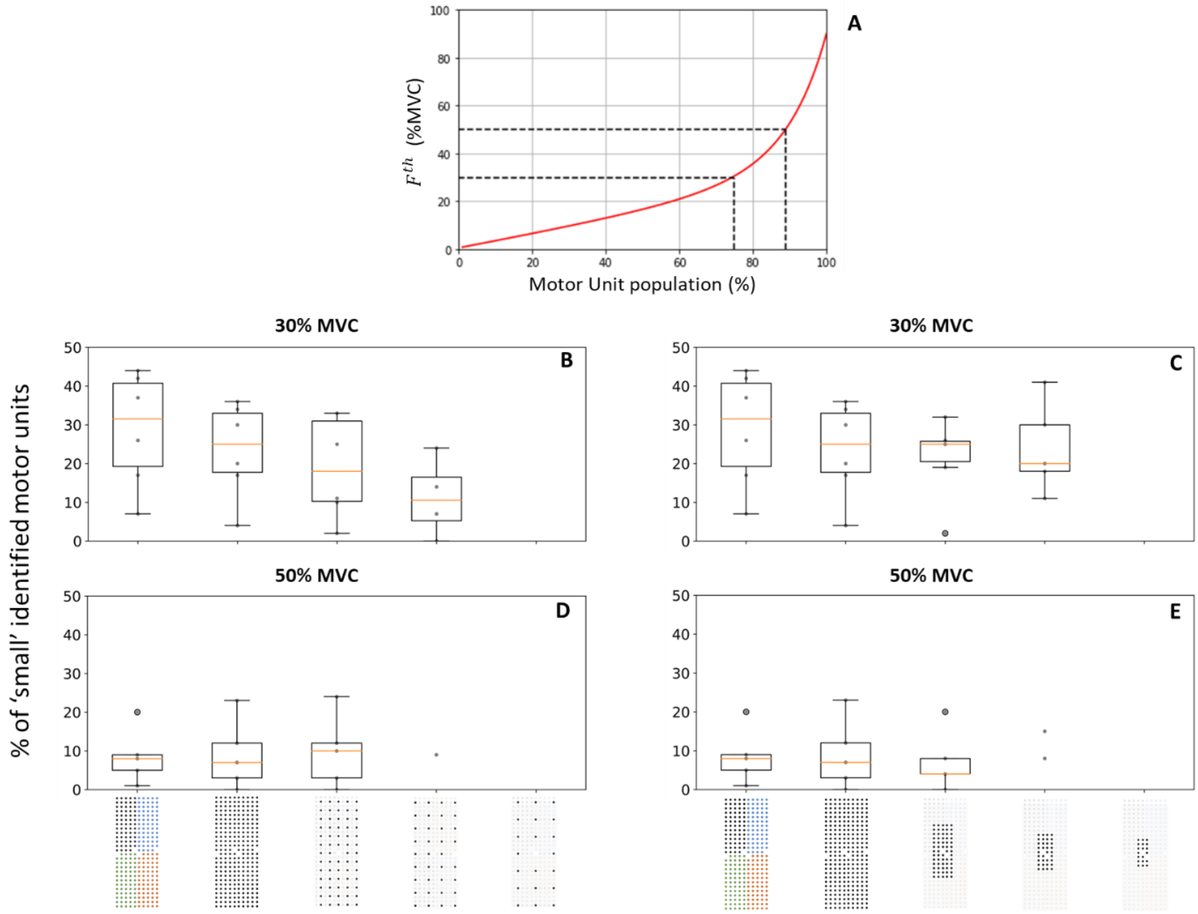

Figure 7: (A) Typical frequency distribution of motor unit force recruitment thresholds in a human TA motor unit pool ranked in ascending order of force recruitment thresholds according to the Methods. The black dashed lines identify the theoretical portions of the population recruited at 30% and 50% MVC. Effect of the grid density (B, D) and grid size (C, E) on the percentage of 'small' motor units identified at 30% (B, C) and 50% MVC (D, E). The boxplots report the results per participant (grey dots) and the median (orange line), quartiles, and 95%-range across participants.

Correlation between MUAPs from adjacent electrodes

Figure 8 reports the effect of electrode density on the level of MUAP correlation ρ between adjacent electrodes for the six participants. The lowest average correlation coefficient ρ calculated between the MUAP with the highest peak to peak amplitude and the MUAPs identified over adjacent electrodes was observed with an IED of 16 mm (ρ = 0.87 ± 0.03 and ρ = 0.88 ± 0.04 at 30% and 50% MVC, respectively). The level of correlation increased with reduced IED (Figure 8B, C), with ρ = 0.96 ± 0.04 and ρ = 0.95 ± 0.05 between the MUAPs from adjacent electrodes with a 4-mm IED at 30% and 50% MVC, respectively.

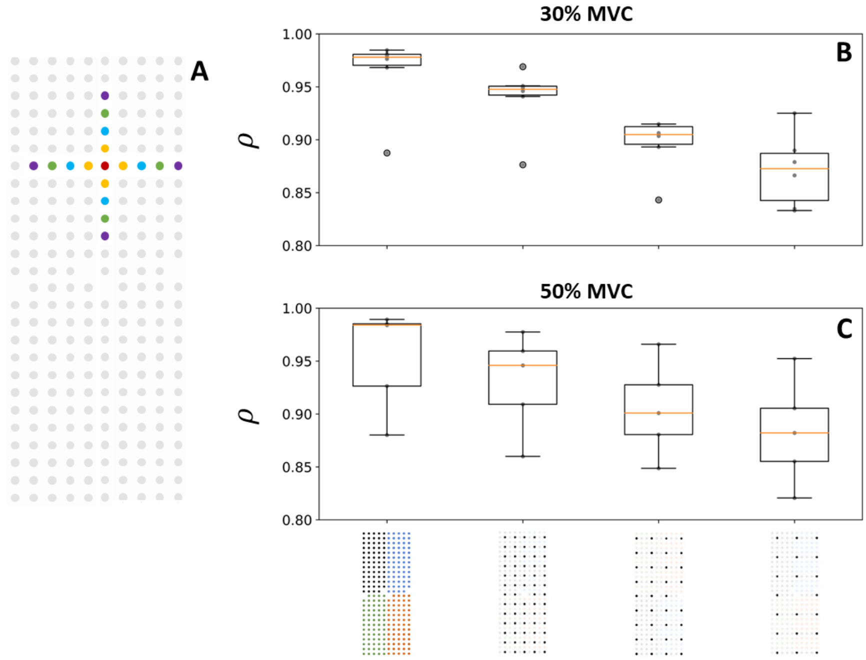

Figure 8: Effect of the electrode density on the MUAP correlation ρ between adjacent electrodes (A) at 30% (B) and 50% MVC (C). The MUAP shape identified over the red electrode was compared to those identified over the four adjacent electrodes located at 4 (orange), 8 (blue), 12 (green) and 16 (purple) mm IED (A). The boxplots report the correlation coefficient ρ per participant (grey dots) and the median (orange line), quartiles, and 95%-range across participants.

Laboratory study with an ultra-dense grid of 400 electrodes

Maximal N of 24 and 14 motor units (PNR > 28 dB) were identified with the ultra-dense grid of 400 electrodes for one participant at 30% and 50% MVC, respectively (Figure 9A), when 8 overlapping subsets of 64 electrodes were decomposed separately. These numbers of units are consistent with the 40×40 mm size of the ultra-dense grid and the results in Figure 5, considering that dry electrodes were used in the second experimental session. Moreover, also consistent with the previous findings, fewer units were identified when the electrode density decreased, with 19 and 4 motor units identified with a 4- and 8-mm IED at 30% MVC, respectively, and with 9 and 5 motor units identified with a 4- and 8-mm IED at 50% MVC, respectively. Although N increased between a 4- and 2-mm IED, with five and four new motor units identified at 30% and 50% MVC respectively (red pulse trains in Figure 9B), the rate of increase of N with electrode density was lower than previously expected (Figure 9C). As previously observed, the correlation between adjacent MUAPs increased from ρ = 0.93 with an 8-mm IED to ρ = 0.98 with a 2-mm IED at 30% MVC, and from ρ = 0.87 with an 8-mm IED to ρ = 0.94 with a 2-mm IED at 50% MVC (Figure 9A). All the motor units identified with the 8-mm and 4-mm IED were also identified with the 4 mm and 2-mm IED grids, respectively. Finally, small motor units were identified when increasing the density from a 8- to 4-mm IED (blue vs black trains in Figure 9B), while most of the smallest units were identified with an IED of 2 mm (red trains in Figure 9B).

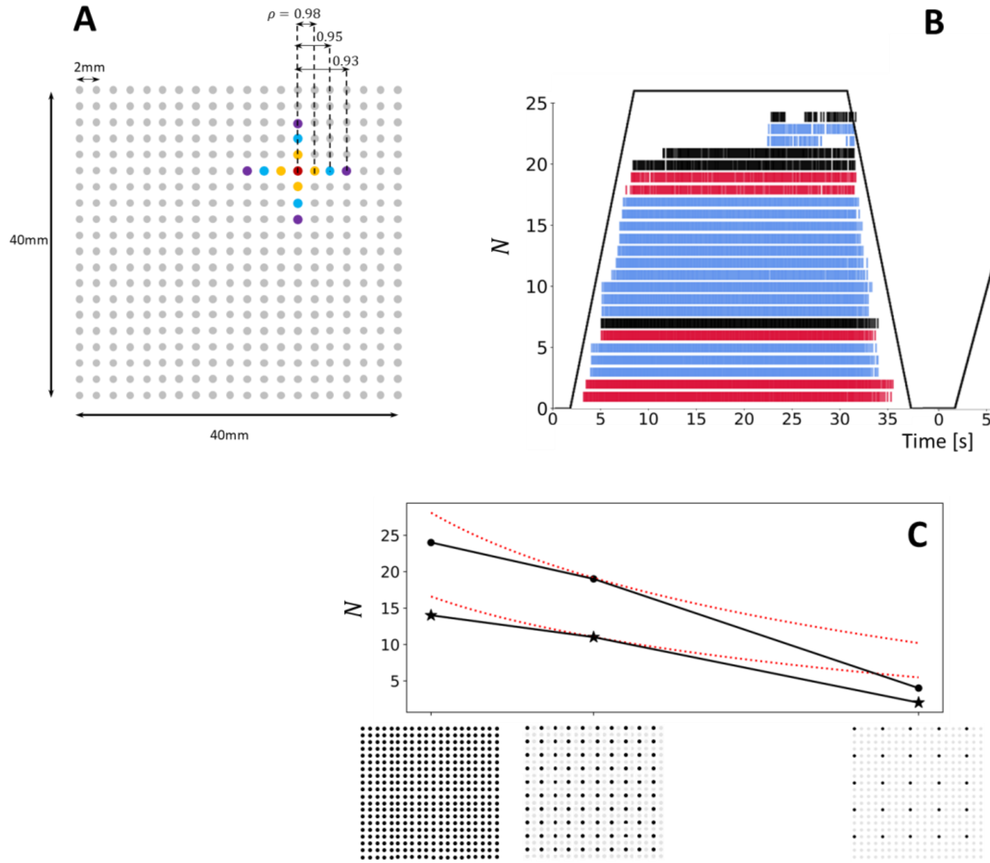

Figure 9: Results for the ultra-dense grid (2 mm IED, 40x40 mm, 400 electrodes). (A) Description of the ultra-dense grid (electrodes represented with grey circles). In average across the 24 identified MUs, the correlation between the MUAPs at a 2 mm (orange), 4 mm (blue), and 8 mm (purple) IED and the MUAP with the highest peak-to-peak amplitude (red) reached ρ = 0.98, 0.95, and 0.93 at 30% MVC, respectively, and 0.94, 0.91, and 0.87 at 50% MVC, respectively. (B) Identified spike trains at 30% (left) and 50% MVC (right). The dark spike trains were identified with an 8 mm IED, the blue trains were additionally identified with the 4 mm IED, and the red trains were identified with 2 mm IED. All the spike trains identified with one grid were also identified with the denser grids. (C) Effect of electrode density on the number of identified motor units at 30% (dots) and 50% MVC (stars). The trendlines from the density analysis in Figure 4B, D computed with the grids of 256 electrodes are also reported (red dotted lines). To maintain consistency with the previous computational and laboratory results, the grid was decomposed as eight partially overlapping subsets of 64 electrodes, as explained in the Methods, to investigate the maximum number of identifiable motor units in this configuration.

Discussion

This study systematically investigated how the design of surface grids of EMG electrodes (grid size and electrode density) impacts the number and the size of the motor units identified with HD-EMG decomposition. Using a combination of computational and experimental approaches, we found that larger and denser grids of electrodes than conventionally used reveal a larger sample of motor units. As those units not identifiable with less dense and smaller grids mostly have a low recruitment threshold, we conclude that denser grids allow the identification of smaller motor units. This is possible because of a better spatial sampling of the MUAP distribution over the skin surface that resulted in a better discrimination among action potentials of different motor units. These results clarify the directions for designing new surface grids of electrodes that could span across the entire surface of the muscle of interest while keeping a high density of electrodes, with IED as low as 2-4 mm. Identifying large sets of small and large motor units is relevant in many research areas related to motor control, such as the investigation of neural synergies (Hug et al., 2022), neuromuscular modelling (Caillet et al., 2022c), or human-machine interfacing (Farina et al., 2021).

The number N of identified motor units increased across participants with the density of electrodes (Figure 4; Figure 8C), the size of the grid (Figure 5), and the number of electrodes (Figure 6). On average, 30 and 19 motor units were identified with the 'conventional' 64-electrode grid (8-mm IED, 32 cm^2 surface area) at 30% and 50% MVC, respectively, which is consistent with several previous studies using similar grid designs (Del Vecchio et al., 2020). By increasing the density of electrodes and size of the grid to arrive to 256 electrodes separated by a 4 mm IED, we identified on average 56 and 45 motor units at 30% and 50% MVC, respectively. We even reached 79 and 59 motor units for one subject (Figure 3), which is substantially more than the numbers of units usually reported in the HD-EMG literature, and twice those obtained with grids of 64 electrodes in this study. Our computational and experimental results showed that the size of the grid is a key factor contributing to the higher number of identified motor units (Figure 2B; Figure 5). According to our simulations, increasing the size of the grid increases the number of identifiable motor units, i.e., the number of motor units with unique sets of MUAPs across electrodes (Figure 2B). We concluded from the simulation that the differences between MUAPs result from the anatomical and physiological differences between adjacent motor units, such as the length of their fibres, the spread of the end plates, or their conduction velocity, as well as from the differences in the tissues interposed between the fibres and each recording electrode (Farina et al., 2004). Larger grids better sample these differences across electrodes, revealing the unique shapes of each motor unit (Farina et al., 2008). The density of electrodes was also found to be a critical factor contributing to increasing the number of identified motor units (Figure 4; Figure 9C). Dense grids especially contribute to identifying the small motor units (Figure 7B; Figure 9B), defined in this study according to their recruitment threshold (Figure 7A) (Henneman and Mendell, 1981; Caillet et al., 2022b). Classically, the decomposition algorithms tend to converge towards the large and superficial motor units that contribute to most of the energy of the EMG signals (Farina and Holobar, 2016). Conversely, action potentials of the smallest motor units tend to have lower energy and are masked by the potentials of the larger units. These factors explain the lowest representation of small low-threshold motor units in available HD-EMG datasets (Caillet et al., 2022a). Increasing the density of electrodes would therefore enable to better sample the action potentials of these small motor units across multiple electrodes, enabling their identification. We however observed that increasing the electrode density did not reveal small motor units anymore during high-force muscle contractions (Figure 7D), potentially because of the large energy of the recorded MUAPs from the large motor units recruited between 30% and 50% MVC. We also showed in one subject that computationally increasing the density of electrodes by spatially resampling the experimental EMG signals (Supplementary Material B) did not reveal any previously hidden motor units.

The number of identified motor units N monotonically increased with the density of electrodes (Figure 4BD), the size of the grid (Figure 5BD) and the number of electrodes (Figure 6), following significant logarithmic trendlines. Remarkably, very similar logarithmic tendencies were obtained at both 30% and 50% MVC in all the analyses. Altogether, these trendlines suggested that the normalized number of identified motor units $\bar{N}$ would grow with an electrode density beyond a 4-mm IED, before reaching a plateau for IEDs of 1-2 mm. We experimentally tested this hypothesis by designing a new grid of 400 dry electrodes separated by an IED of 2 mm. While more motor units were identified at 2 mm than 4 mm IED, as expected, the rate of increase between 4-mm and 2-mm IED was lower than predicted by the trendlines (Figure 9C). We explained this result by demonstrating that the level of correlation between MUAPs identified over adjacent electrodes, which was >0.95 at both contraction levels with 4-mm IED (Figure 8), tended to 1 with further increasing electrode density (Figure 9A). Therefore, the high level of information shared between adjacent electrodes in ultra-dense grids (IED < 2 mm) limits the percentage of identifiable motor units (Farina and Holobar, 2016). According to these results, we consider that optimal designs of surface grids of electrodes for identifying individual motor units would involve a surface that cover the muscle of interest with an IED of 2 to 4 mm, depending on the size of the muscle. It cannot be excluded, however, that the high correlation between adjacent electrodes with a 2-mm IED was partly due to the grid design and can be improved by reducing the electric crosstalk between electrodes, e.g., by reducing the electrode area.

Another important factor for the identification of individual motor units is the quality of the identified pulse trains, estimated by the PNR (Holobar et al., 2014) or the silhouette value. In this study, we showed that the quality of the identified motor units (i.e., decomposition accuracy) increased when increasing the density of electrodes or the size of the grid, with PNR reaching on average 37-38 dB across participants with the grid of 256 electrodes (Supplementary Material C). A greater average PNR implies the need of less manual editing following the automatic decomposition (Hug et al., 2021b). The better spike train estimate depends on the better signal to noise ratio following the inversion of the mixing matrix since the pulse train of each motor unit is computed by projecting the extended, whitened signals on the separation vector (Holobar and Farina, 2014; Farina and Holobar, 2016; Negro et al., 2016). Likewise, the PNR substantially increased after we computationally increased the number of electrodes by spatially resampling the EMG signals. This practical result is of interest for most of the physiological studies that require a lengthy processing time to visually check and manually correct the pulse trains of all the motor units (Hug et al., 2021b).

Finally, by independently decomposing subsets of 64 electrodes, we increased both the total number and the percentage of small motor units identified from highly populated grids of 256 electrodes, compared to the simultaneous decomposition of all available observations (Figure 7B, C). This was likely due to the lower ratio of large motor units sampled by each subset of electrodes, allowing the algorithm to converge to smaller motor units that contributed to the signal (Figure 7B, C). According to Supplementary Material A, the plateauing behaviour previously observed in Figure 4 to Figure 6 is expected to be more pronounced when all the available signals are simultaneously decomposed. It should however be noted that the simulation results were obtained independently of a specific decomposition algorithm, as previously proposed by Farina et al (2008). On the other hand, the experimental results are based on a specific algorithm. Interestingly, however, the simulation and laboratory results were fully consistent and in agreement, indicating that the difference in shape of the spatially sampled MUAPs is the main factor influencing EMG decomposition.

Conclusion

By increasing the density and the number of electrodes, and the size of the grids, we increased the number of identifiable and experimentally identified motor units. The identified motor units had pulse trains with high PNR, limiting the manual processing time. Moreover, we identified a higher percentage of small motor units, which are classically filtered out with the current conventional grid designs. In this way, a maximum of 79 motor units (PNR > 28 dB; mean: 36 dB), including 40% of small motor units, were identified, which is a substantially greater sample than previously shown with smaller and less dense grids. From these results, we encourage researchers to develop and apply larger and denser EMG grids to cover the full muscle of interest with IEDs as small as 2 mm. This approach increases the sample of motor units that can be experimentally investigated with non-invasive techniques.

References:

Caillet AH, Phillips ATM, Farina D, Modenese L (2022a) Estimation of the firing behaviour of a complete motoneuron pool by combining electromyography signal decomposition and realistic motoneuron modelling. PLoS Comput Biol 18:e1010556.

Caillet AH, Phillips ATM, Farina D, Modenese L (2022b) Mathematical relationships between spinal motoneuron properties. Elife 11.

Caillet AH, Phillips ATM, Carty CP, Farina D, Modenese L (2022c) Hill-type computational models of muscle-tendon actuators: a systematic review. bioRxiv:2022.2010.2014.512218.

Churchland MM, Shenoy KV (2007) Temporal complexity and heterogeneity of single-neuron activity in premotor and motor cortex. J Neurophysiol 97:4235-4257.

Del Vecchio A, Negro F, Felici F, Farina D (2017) Associations between motor unit action potential parameters and surface EMG features. J Appl Physiol (1985) 123:835-843.

Del Vecchio A, Holobar A, Falla D, Felici F, Enoka RM, Farina D (2020) Tutorial: Analysis of motor unit discharge characteristics from high-density surface EMG signals. J Electromyogr Kinesiol 53:102426.

Enoka RM (2019) Physiological validation of the decomposition of surface EMG signals. J Electromyogr Kinesiol 46:70-83.

Farina D, Holobar A (2016) Characterization of Human Motor Units From Surface EMG Decomposition. Proceedings of the Ieee 104:353-373.

Farina D, Merletti R, Enoka RM (2004) The extraction of neural strategies from the surface EMG. J Appl Physiol (1985) 96:1486-1495.

Farina D, Negro F, Gazzoni M, Enoka RM (2008) Detecting the unique representation of motor-unit action potentials in the surface electromyogram. J Neurophysiol 100:1223-1233.

Farina D, Negro F, Muceli S, Enoka RM (2016) Principles of Motor Unit Physiology Evolve With Advances in Technology. Physiology (Bethesda) 31:83-94.

Farina D, Vujaklija I, Brånemark R, Bull AMJ, Dietl H, Graimann B, Hargrove LJ, Hoffmann KP, Huang HH, Ingvarsson T, Janusson HB, Kristjánsson K, Kuiken T, Micera S, Stieglitz T, Sturma A, Tyler D, Weir RFF, Aszmann OC (2021) Toward higher-performance bionic limbs for wider clinical use. Nat Biomed Eng.

Gallego JA, Perich MG, Chowdhury RH, Solla SA, Miller LE (2020) Long-term stability of cortical population dynamics underlying consistent behavior. Nat Neurosci 23:260-270.

Heckman CJ, Enoka RM (2012) Motor unit. Compr Physiol 2:2629-2682.

Henneman E, Mendell LM (1981) Functional Organization of Motoneuron Pool and its Inputs. In: Comprehensive Physiology, pp 423-507.

Holobar A, Farina D (2014) Blind source identification from the multichannel surface electromyogram. Physiol Meas 35:R143-165.

Holobar A, Minetto MA, Farina D (2014) Accurate identification of motor unit discharge patterns from high-density surface EMG and validation with a novel signal-based performance metric. J Neural Eng 11:016008.

Hug F, Del Vecchio A, Avrillon S, Farina D, Tucker K (2021a) Muscles from the same muscle group do not necessarily share common drive: evidence from the human triceps surae. J Appl Physiol (1985) 130:342-354.

Hug F, Avrillon S, Sarcher A, Del Vecchio A, Farina D (2022) Correlation networks of spinal motor neurons that innervate lower limb muscles during a multi-joint isometric task. J Physiol.

Hug F, Avrillon S, Del Vecchio A, Casolo A, Ibanez J, Nuccio S, Rossato J, Holobar A, Farina D (2021b) Analysis of motor unit spike trains estimated from high-density surface electromyography is highly reliable across operators. J Electromyogr Kinesiol 58:102548.

Jun JJ et al. (2017) Fully integrated silicon probes for high-density recording of neural activity. Nature 551:232-236.

Konstantin A, Yu T, Le Carpentier E, Aoustin Y, Farina D (2020) Simulation of Motor Unit Action Potential Recordings From Intramuscular Multichannel Scanning Electrodes. IEEE Transactions on Biomedical Engineering 67:2005-2014.

Muceli S, Poppendieck W, Holobar A, Gandevia S, Liebetanz D, Farina D (2022) Blind identification of the spinal cord output in humans with high-density electrode arrays implanted in muscles. Science advances 8:eabo5040.

Muceli S, Poppendieck W, Negro F, Yoshida K, Hoffmann KP, Butler JE, Gandevia SC, Farina D (2015) Accurate and representative decoding of the neural drive to muscles in humans with multi-channel intramuscular thin-film electrodes. J Physiol 593:3789-3804.

Negro F, Muceli S, Castronovo AM, Holobar A, Farina D (2016) Multi-channel intramuscular and surface EMG decomposition by convolutive blind source separation. J Neural Eng 13:026027.

Steinmetz NA, Koch C, Harris KD, Carandini M (2018) Challenges and opportunities for large-scale electrophysiology with Neuropixels probes. Curr Opin Neurobiol 50:92-100.

Stringer C, Pachitariu M, Steinmetz N, Reddy CB, Carandini M, Harris KD (2019) Spontaneous behaviors drive multidimensional, brainwide activity. Science 364:255.